

Superconducting properties in a candidate topological nodal line semimetal SnTaS_2 with a centrosymmetric crystal structure

Dong-Yun Chen^{1,2,3}, Yuelong Wu,¹ Lei Jin,⁴ Yongkai Li,^{2,3} Xiaoxiong Wang,¹ Junxi Duan,^{2,3} Junfeng Han,^{2,3} Xiang Li,^{2,3} Yun-Ze Long,¹ Xiaoming Zhang,⁴ Dong Chen^{1,*} and Bing Teng^{1,†}

¹College of Physics, Qingdao University, Qingdao 266071, China

²Key Laboratory of Advanced Optoelectronic Quantum Architecture and Measurement, Ministry of Education, School of Physics, Beijing Institute of Technology, Beijing 100081, China

³Micronano Centre, Beijing Key Lab of Nanophotonics and Ultrafine Optoelectronic Systems, Beijing Institute of Technology, Beijing 100081, China

⁴School of Materials Science and Engineering, Hebei University of Technology, Tianjin 300130, China



(Received 4 May 2019; published 20 August 2019)

We report the magnetization, the electrical resistivity, specific heat measurements, and band structure calculations of the layered superconductor SnTaS_2 . The experiments are performed on single crystals grown by the chemical vapor transport method. The resistivity and magnetic susceptibility indicate that SnTaS_2 is a type-II superconductor with the transition temperature $T_c = 3$ K. The upper critical field (H_{c2}) shows large anisotropy for the magnetic field parallel to the ab plane ($H//ab$) and the c axis ($H//c$), and the temperature dependence of H_{c2} for $H//ab$ shows an obvious unconventional upward feature at low temperature. The band structure of SnTaS_2 shows several band crossings near the Fermi level, which form three nodal lines in the $k_z = 0$ plane resulting in drumheadlike surface states when spin-orbit coupling is not considered. These results indicate that SnTaS_2 is a superconductor with a possible topological nodal line semimetal character.

DOI: [10.1103/PhysRevB.100.064516](https://doi.org/10.1103/PhysRevB.100.064516)

I. INTRODUCTION

Superconductors with nontrivial band structure have attracted much attention due to the possibility of realizing some novel quantum states, such as topological superconductors and Majorana fermions [1,2]. Nontrivial band structure has been found in both topological insulators and topological semimetals [1,3–5]. Topological semimetals can be further classified according to the configuration of band crossing near the Fermi level, including Dirac semimetals, Weyl semimetals, nodal line semimetals, etc. [6–11]. Superconductivity can be combined with the novel band structure by charge carrier doping or applying external pressure on topological materials. For example, the topological insulator Bi_2Se_3 has been found to be superconducting when intercalated by Cu, Sr, or Nb atoms [12–14] or subjected to high pressure [15]. The Dirac semimetal Cd_3As_2 and the type-II Weyl semimetal WTe_2 can be induced as superconductors under high pressure [16–18]. Besides, some topological materials themselves are superconductors. The type-II Weyl semimetal MoTe_2 has a superconducting transition with $T_c = 0.1$ K, and the T_c can be dramatically enhanced to 8.2 K with high pressure [19]. PbTaSe_2 has been found to be a superconducting topological nodal line semimetal with a noncentrosymmetric structure [20,21]. The later category of aforementioned superconductors does not suffer topological state shift from charge carrier doping or high pressure, providing an excellent playground for research-ing superconductivity with nontrivial band topology.

The layered compound SnTaS_2 , which is isoelectronic with PbTaSe_2 , is another superconductor identified as early as 1973 [22]. Although the critical temperature for SnTaS_2 ($T_c = 2.8$ K) has been reported [22,23], more detailed superconducting properties are still unknown. Moreover, we notice that SnTaS_2 has a centrosymmetric structure, which is different from that of PbTaSe_2 . Whether the centrosymmetric SnTaS_2 can host the topological nontrivial band structure is also unknown. In this paper, we have systemically investigated the superconducting properties and the electronic structure of SnTaS_2 . The magnetization, electric transport, and specific heat properties are studied in detail on the single crystal samples. We find large anisotropy in the upper critical field and coherence length. The temperature dependence of the upper critical field has an obvious upward feature for the magnetic field parallel to the ab plane. Analysis of the specific heat shows that SnTaS_2 is a moderately coupled superconductor. Using first-principles calculations, we find that centrosymmetric SnTaS_2 exhibits a topological nodal line band structure when spin-orbit coupling (SOC) is not included. It features three nodal lines centering the K point near the Fermi level, along with drumheadlike surface states corresponding to them. These properties are similar to those of PbTaSe_2 . Our work suggests that SnTaS_2 is another system for investigating the novel properties of superconductors with topological nodal-line fermions.

II. EXPERIMENT AND METHODS

The single crystals of SnTaS_2 were grown by the chemical vapor transport method with iodine as the transport agent. Polycrystalline $\text{Sn}_{0.33}\text{TaS}_2$ was synthesized previously by the

*dchen@qdu.edu.cn

†5108tb@163.com

solid state reaction of Sn, Ta, and S powders in an evacuated quartz tube at 850 °C. The obtained $\text{Sn}_{0.33}\text{TaS}_2$ polycrystals were mixed with Sn powders with an element ratio of Sn:Ta:S = 1.2:1:2 and sealed in an evacuated quartz tube together with iodine (3 mg/cm³ in concentration). The excess Sn was used to restrain the appearance of $\text{Sn}_{0.33}\text{TaS}_2$. The quartz tube was then put into a two-zone furnace with 1000 °C in the hot zone and 970 °C in the cold zone for 2 weeks. Thin plate-shaped single crystals were obtained with typical dimensions of $3 \times 3 \times 0.05$ mm³. The crystal structure of the obtained crystals was characterized by x-ray diffraction (XRD) on a Rigaku Smartlab x-ray diffractometer with Cu $K\alpha$ radiation at room temperature. The atomic ratio was determined by Oxford energy-dispersive x-ray (EDX) spectroscopy analysis. The magnetization, resistivity, and specific heat of the samples were measured using a Quantum Design Physical Property Measurement System.

The band structure calculations were performed based on the density functional theory (DFT), as implemented in the Vienna *ab initio* simulation package (VASP) [24]. The generalized gradient approximation with the realization of the Perdew-Burke-Ernzerhof functional was adopted for the exchange-correlation potential [25]. The cutoff energy was set to be 450 eV and the Brillouin zone was sampled with a $13 \times 13 \times 5$ Γ -centered k mesh. The energy convergence criterion was chosen to be 10^{-6} eV. The surface states were computed by using the Wannier_tools package [26].

III. RESULTS AND DISCUSSION

SnTaS_2 has a layered hexagonal structure (space group $P6_3/mmc$) with the lattice parameters $a = b = 3.309$ Å and $c = 17.450$ Å. The layered structure is formed by the alternative stacking of TaS_2 and Sn layers, as shown in Fig. 1(a). It should be noted that SnTaS_2 preserves the inversion and twofold screw rotation symmetries. Figure 1(b) is the XRD pattern of the maximum surface of a platelike single crystal. All of the peaks can be indexed as the (00 l) reflections of SnTaS_2 , indicating the single crystals perfectly oriented along the c axis. The crystals can be further confirmed as SnTaS_2 by powder XRD and EDX measurements.

Figure 1(c) displays the typical temperature dependence of the resistivity for SnTaS_2 single crystals with current applied in the ab plane. The resistivity shows a metallic behavior and the residual resistivity ratio $\text{RRR} = \rho(300 \text{ K})/\rho(4 \text{ K})$ is as high as 380, indicating the high quality of the samples. The linear temperature dependence of the resistivity at high temperature suggests the dominance of electron-phonon scattering. As shown in the inset of Fig. 1(c), the resistivity has a sharp superconducting transition, and the critical temperature T_c can be determined as 3.0 K using the criterion of the 50% point on the transition curve. To further demonstrate the superconductivity of the samples, we measured the dc susceptibility in the zero-field-cooling (ZFC) and field-cooling (FC) processes with a magnetic field of 10 Oe parallel to the ab plane, as displayed in Fig. 1(d). The demagnetization effect is not considered due to the thin plate-shaped sample with the magnetic field parallel to the sample plane. The T_c determined from the susceptibility curve is about 2.97 K, close to that determined from resistivity data. The superconducting shielding

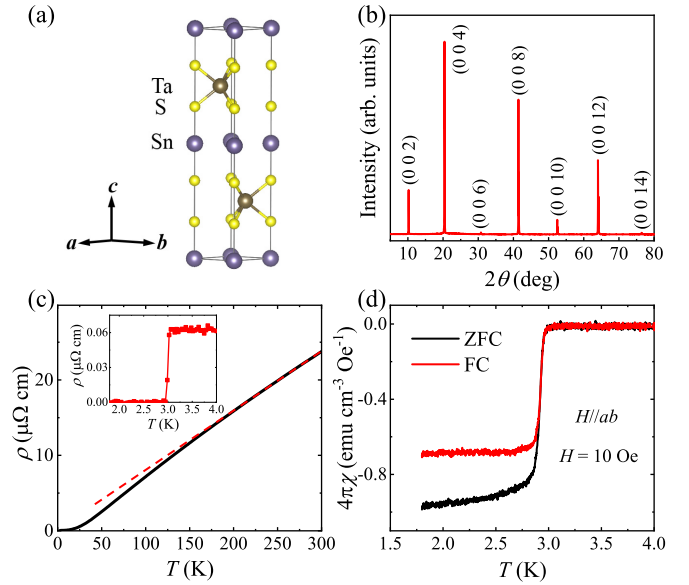


FIG. 1. (a) Crystal structure of SnTaS_2 . (b) The XRD pattern of SnTaS_2 single crystals with (00 l) reflections. (c) The temperature dependence of the resistivity with current flowing in the ab plane. The straight dashed line is the guide to the linear behavior of the resistivity in high temperature. The inset shows the superconducting transition of resistivity. (d) The zero-field-cooling (ZFC) and field-cooling (FC) magnetic susceptibility curves measured with a magnetic field of 10 Oe and parallel to the ab plane.

volume fraction at 1.8 K is close to 100%. In addition, the FC curve is not coincident with the ZFC curve, suggesting a type-II superconductor. However, the FC curve is not much larger than the ZFC curve, indicating few vortices pinning.

To estimate the anisotropic lower critical field (H_{c1}), the zero-field-cooled magnetization $M(H)$ curves were measured with $H//ab$ and $H//c$, as shown in Figs. 2(a) and 2(c), respectively. The values of H_{c1} are determined as the points for $M(H)$ deviating 5% from the linear fitted curves. To get the accurate values of H_{c1} , the demagnetization effect should be considered. For a perfectly diamagnetic superconductor, the magnetic field lines are excluded from the inside of the sample and have higher density on the outside. This makes a higher field that the sample feels around it and a more pronounced diamagnetization slope, i.e., $M/H_a = -1/(1 - N)$, where N is the demagnetization factor. For the thin plate-shaped sample, N is almost 0 for the magnetic field parallel to the sample's surface and is nearly 1 when the magnetic field is perpendicular to the surface. Thus, for the thin SnTaS_2 plates, the H_{c1} for $H//ab$ (H_{c1}^{ab}) can be determined directly from the magnetization curves without demagnetization correction, as shown in Fig. 2(b). By contrast, the demagnetization correction cannot be neglected when we determine the H_{c1} for $H//c$ (H_{c1}^c). To calculate the demagnetization factor N , we employ the following relation [27]:

$$N = 1 - 1/\left(1 + q_{\text{disk}} \frac{a}{c}\right), \quad (1)$$

$$q_{\text{disk}} = \frac{4}{3\pi} + \frac{2}{3\pi} \tanh \left[1.27 \frac{c}{a} \ln \left(1 + \frac{a}{c} \right) \right], \quad (2)$$

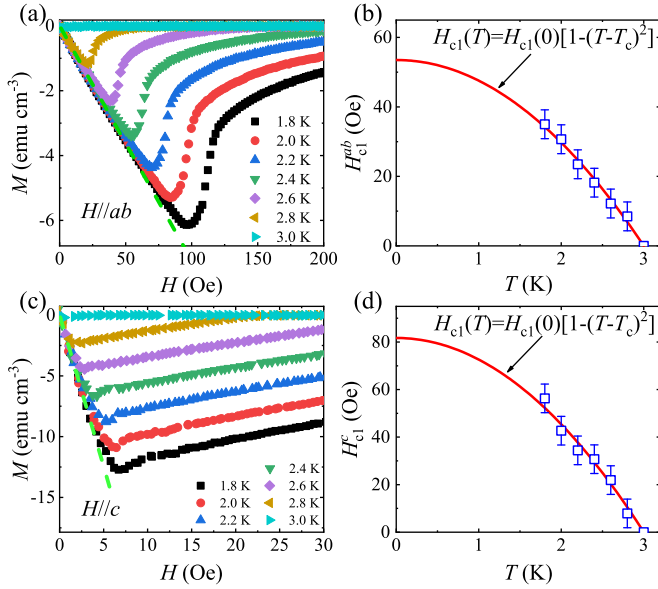


FIG. 2. (a) and (c) The zero-field-cooled magnetization $M(H)$ curves at different temperatures with the magnetic field parallel to the ab plane and the c axis, respectively. The dashed lines are the linear fit to the 2 K curves in the low-field range. (b) and (d) The lower critical field for the magnetic field parallel to the ab plane and the c axis, respectively, with the fit lines using the equation $H_{c1}(T) = H_{c1}(0)[1 - (T/T_c)^2]$. The demagnetization correction is considered in H_{c1}^c .

where a and c are the dimension perpendicular to the magnetic field and the thickness of the sample, respectively. Here, the demagnetization correction has been considered in determining the values of H_{c1}^c in Fig. 2(d) with $N \approx 0.9473$. Both the H_{c1}^c and the H_{c1}^{ab} data can be fitted using $H_{c1}(T) = H_{c1}(0)[1 - (T/T_c)^2]$. The lower critical fields at zero temperature for the two directions are $H_{c1}^{ab}(0) = 53.5$ Oe and $H_{c1}^c(0) = 81.7$ Oe, respectively.

The low-temperature resistivity under various magnetic fields with $H//c$ and $H//ab$ are presented in Figs. 3(a) and 3(c), respectively. The superconducting transition is very sharp for the zero-field curve and is broadened lightly by the applied fields. With the 50% criterion to determine the transition temperatures, the upper critical fields for $H//c$ (H_{c2}^c) and $H//ab$ (H_{c2}^{ab}) as the functions of temperature are given in Figs. 3(b) and 3(d), respectively. The temperature dependence of H_{c2}^c can be well fitted with the Ginzberg-Landau (GL) equation $H_{c2}(T) = H_{c2}(0)(1 - t^2)/(1 + t^2)$, where $t = T/T_c$. The upper critical field at $T = 0$ K for $H//c$ is accordingly estimated as $H_{c2}^c(0) = 203.6$ Oe. For $H//ab$, the temperature dependence of H_{c2}^{ab} has an obvious upward feature and deviates from the GL equation for $T < 2.5$ K. This upward feature for $H_{c2}^{ab}(T)$ is also found in PbTaSe_2 [20,28–30], where the upper critical field can be roughly fitted by the equation $H_{c2}(T) = H_{c2}(0)(1 - t^{3/2})^{3/2}$. However, the fitting curve using this formula is also lower than the $H_{c2}^{ab}(T)$ data in the low-temperature region [Fig. 3(d)], indicating the upward feature in SnTaS_2 is more obvious than that of PbTaSe_2 .

The enhancement of H_{c2} at low temperatures has several possible origins, such as (i) dimensional crossover [31],

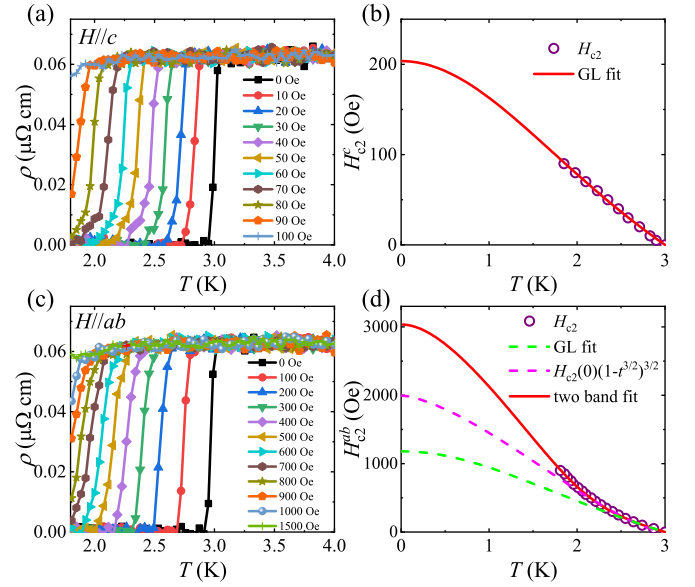


FIG. 3. (a) and (c) The low-temperature $\rho(T)$ curves under different magnetic fields for $H//c$ and $H//ab$, respectively. (b) The temperature dependence of the upper critical field extracted from the resistivity curves with $H//c$. The data are fitted by the GL equation. (d) The temperature dependence of the upper critical field extracted from the resistivity curves with $H//ab$. The data are fitted by three different equations.

(ii) the presence of impurities and disorder [32,33], (iii) the multiband effect [34], (iv) the melting of the vortex lattice associate with quantum critical point [35], and (v) the non-local effect in the clean limit [36]. The dimensional crossover means that the superconductor changes from a bulk superconductor to a stacked array of two-dimensional superconducting layers with the coherence length perpendicular to the layers (ξ_c) getting smaller than the distance between adjacent layers with decreasing temperature. This theory has been used to explain the upward curvature in $H_{c2}^{ab}(T)$ of organic-molecules-intercalated 2H-TaS_2 [37,38], in which the H_{c2}^{ab} 's can exceed the Pauli paramagnetic limit at moderate temperatures and the coherence lengths are comparable with the TaS_2 layer distance. In our case, the H_{c2}^{ab} is much smaller than the Pauli paramagnetic limiting field ($\mu_0 H_P = 5.5$ T) down to 1.8 K, and the ξ_c is much larger than the layer distance (see below). These facts demonstrate that the layers in SnTaS_2 are not decoupled and it is a bulk superconductor. On the other hand, the high value of RRR = 380 indicates the high quality and low density of defects in our samples. This excludes the possibility of the scattering by impurities and supports the nonlocal effect scenario. The current properties of SnTaS_2 show no trace for the quantum critical point. The result of DFT computations discussed later shows that several bands cross the Fermi level. Therefore, the multiband effect and the nonlocal effect are the most likely origins for the upward curvature of $H_{c2}^{ab}(T)$.

To estimate $H_{c2}^{ab}(0)$, we try to fit the $H_{c2}^{ab}(T)$ data using the equation for a two-band superconductor [34], i.e.,

$$a_0[\ln t + U(t)][\ln t + U(\eta h)] + a_1[\ln t + U(h)] + a_2[\ln t + U(\eta h)] = 0, \quad (3)$$

TABLE I. The superconducting parameters of the SnTaS₂ single crystal.

	$H//ab$	$H//c$
$H_{c1}(0)$ (Oe)	53.5	81.7
$H_{c2}(0)$ (Oe)	3034	203.6
$\xi(0)$ (nm)	127	8.5
$\kappa(0)$	7.58	5.07
$\lambda(0)$ (nm)	64.4	962.4
$\gamma_{\text{anis}}(0)$		14.9
$\Delta C/\gamma T_c$		1.23
Θ_D (K)		154.4
λ_{ep}		0.66

where $t = T/T_c$, $h = \frac{H_{c2}D_1}{2\Phi_0 T}$, $\eta = \frac{D_2}{D_1}$, $U(x) = \psi(x + \frac{1}{2}) - \psi(\frac{1}{2})$, $a_0 = 2(\lambda_{11}\lambda_{22} - \lambda_{12}\lambda_{21})/\lambda_0$, $a_1 = 1 + (\lambda_{11} - \lambda_{22})/\lambda_0$, $a_2 = 1 - (\lambda_{11} - \lambda_{22})/\lambda_0$, and $\lambda_0 = \sqrt{(\lambda_{11} - \lambda_{22})^2 + 4\lambda_{12}\lambda_{21}}$. $\psi(x)$ is the digamma function. D_1 and D_2 are the intraband diffusivities of each band. λ_{11} and λ_{22} are the intraband coupling constants, whereas λ_{12} and λ_{21} are the interband coupling constants. As shown in Fig. 3(d), the experimental data can be well fitted by the two-band formula, which gives $H_{c2}^{ab}(0) = 3034$ Oe. The $H_{c2}^{ab}(0)$ is much lower than the Pauli limiting field, suggesting the upper critical field is limited by the orbital effect. The anisotropic ratio of H_{c2} , $\gamma_{\text{anis}}(0) = H_{c2}^{ab}(0)/H_{c2}^c(0)$, is as large as 14.9, larger than those of 2H-TaS₂ ($\gamma_{\text{anis}} = 6$) and PbTaSe₂ ($\gamma_{\text{anis}} = 11.6$) [29,38].

Based on the GL theory, the anisotropic coherence length is given by $H_{c2}^{ab} = \Phi_0/(2\pi\xi_{ab}\xi_c)$ and $H_{c2}^c = \Phi_0/(2\pi\xi_{ab}^2)$, where Φ_0 is the flux quantum [39]. Accordingly, the anisotropic GL coherence length at zero temperature can be determined to be $\xi_{ab}(0) = 127$ nm and $\xi_c(0) = 8.5$ nm, and the anisotropic ratio is $\xi_{ab}/\xi_c = 14.9$. As mentioned above, ξ_c is much larger than the TaS₂ layer distance (~ 8.7 Å), indicating the bulk superconductivity of this system. The GL parameter $\kappa_i(0)$ along the i direction can be obtained by the equation $H_{c2}^i(0)/H_{c1}^i(0) = 2\kappa_i^2(0)/\ln\kappa_i(0)$. The GL parameter $\kappa_i(0)$ is related with the anisotropic GL penetration length $\lambda_i(0)$ and the coherence length $\xi_i(0)$ by the equations $\kappa_c(0) = \lambda_{ab}(0)/\xi_{ab}(0)$ and $\kappa_{ab}(0) = \lambda_{ab}(0)/\xi_c(0) = [\lambda_{ab}(0)\lambda_c(0)/\xi_{ab}(0)\xi_c(0)]^{1/2}$, in which $\xi_{ab}/\xi_c = \lambda_c/\lambda_{ab}$. With these relations, the GL parameter $\kappa_i(0)$ and the anisotropic $\lambda_i(0)$ can be determined, as listed in Table I.

To further investigate the superconducting properties of SnTaS₂, we performed specific heat measurements and analysis. The low-temperature specific heat under the fields of $\mu_0H = 0$ and 1 T are demonstrated as the relationships of C/T versus T^2 in Fig. 4. With $\mu_0H = 0$ T, the specific heat shows a sharp jump at $T_c = 2.88$ K, which is determined by the isoentropic method shown in the inset. The superconducting transition is completely suppressed by a magnetic field of 1 T, and the $C/T - T^2$ curve under $\mu_0H = 1$ T can be well fitted by the formula $C/T = \gamma + \beta T^2 + \delta T^4$. The fit yields the normal state Sommerfeld coefficient $\gamma = 4.45$ mJ/mol K², and the phonon-specific coefficient $\beta = 2.11$ mJ/mol K⁴. The value of $\Delta C/\gamma T_c$ is estimated as 1.23, which is smaller than the value of the BCS theory (1.43). With the formula

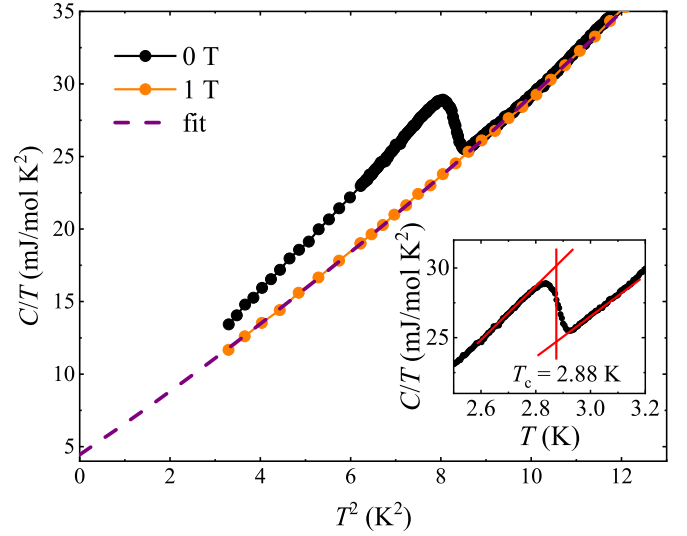


FIG. 4. The specific heat divided by temperature (C/T) as the function of T^2 with $\mu_0H = 0$ and 1 T. The curve for $\mu_0H = 1$ T is fitted by the relation $C/T = \gamma + \beta T^2 + \delta T^4$. The inset shows the isoentropic method for T_c determination.

$\Theta_D = [(12/5\beta)\pi^4 n N_A k_B]^{1/3}$, where $n = 4$ for SnTaS₂ and N_A is the Avogadro constant, the Debye temperature is estimated as $\Theta_D = 154.4$ K. The electron-phonon coupling constant λ_{ep} can be calculated using McMillan's formula [40]:

$$\lambda_{ep} = \frac{1.04 + \mu^* \ln(\Theta_D/1.45T_c)}{(1 - 0.62\mu^*) \ln(\Theta_D/1.45T_c) - 1.04}. \quad (4)$$

The value of λ_{ep} is 0.66 assuming $\mu^* = 0.13$. This value is smaller than 1.0, the minimum value of strong coupling, indicating SnTaS₂ is a moderately coupled superconductor. Both the values of Θ_D and λ_{ep} are close to those of PbTaSe₂ [20,28,29]. With these results, the noninteracting density of states at the Fermi level can be calculated by $N(E_F) = 3\gamma/[\pi^2 k_B^2 (1 + \lambda_{ep})]$, which gives $N(E_F) = 1.14$ states eV⁻¹ per formula unit. It can be noticed that the above parameters are different from those in the previous work [23]. This discrepancy may be due to the different sample quality caused by the changed growth conditions.

In view of the similarity of the element component of SnTaS₂ with the topological nodal line semimetal PbTaSe₂, we study the band structure of SnTaS₂ through the first-principles calculations. Figure 5(a) is the schematic diagram for the bulk and the (001)-surface Brillouin zone of SnTaS₂. Figure 5(b) clearly manifests a metallic band structure with several bands crossing the Fermi level. As shown by the enlarged band structure in Fig. 5(c), there exist six band-crossing points at M-K and K-Γ paths near the Fermi level without SOC in account. By performing more careful calculations on the band structure nearby, we find these band-crossing points are not isolated but belong to three nodal lines centering the K point in the $k_z = 0$ plane, as shown in Fig. 5(d). This indicates SnTaS₂ is a topological nodal line semimetal in the absence of SOC. In addition, the drumheadlike surface states from the nodal lines are quite visible, as pointed out by the arrows in Fig. 5(e). When SOC is included, the nodal lines in SnTaS₂ are gapped, as shown in Fig. 5(f). The sizes of SOC gaps in

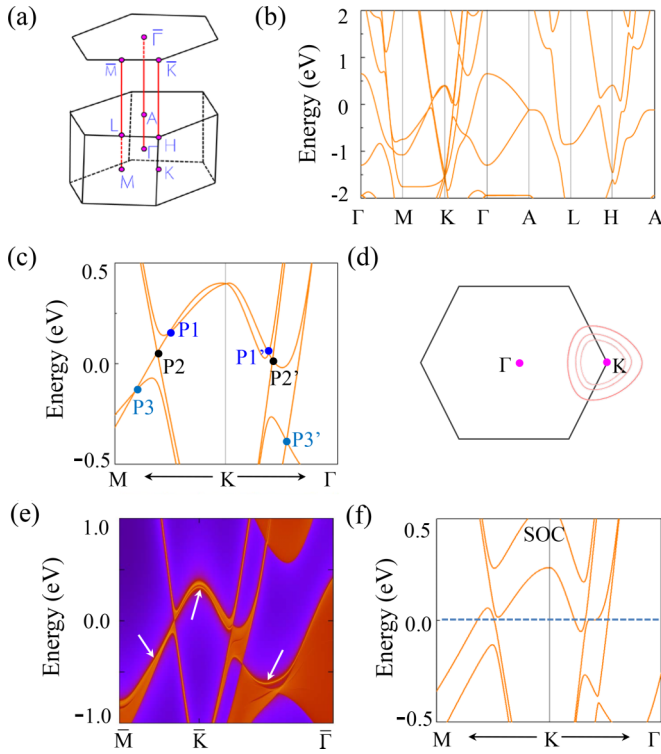


FIG. 5. (a) Bulk and (001)-surface Brillouin zone of SnTaS₂. (b) Electronic band structure of SnTaS₂ without SOC. (c) Enlarged band structure along the M-K and K- Γ paths. (d) Illustration of the three nodal lines centering the K point in the $k_z = 0$ plane. (e) The Sn-terminated (001) surface band structure for SnTaS₂. The drumheadlike surface states are pointed out by white arrows. (f) Electronic band structure of SnTaS₂ with SOC included.

SnTaS₂ are in the range of 15–180 meV, which are comparable with typical nodal line materials such as TiB₂, Cu₃PdN, Mg₃Bi₂, and CaAgAs [41–45]. From Figs. 5(b) and 5(f), we can observe several electronlike and holelike bands cross the Fermi level, consistent with the multiband scenario which is a possible origin for the upward curvature of $H_{c2}^{ab}(T)$ in our samples. The density of states at the Fermi level calculated from the band structure is 1.04 states eV⁻¹ per formula unit with SOC, in good agreement with the value obtained from specific heat measurements.

It is interesting that, similar to PbTaSe₂, SnTaS₂ is also a superconducting nodal line semimetal, which is isoelectronic with but not isostructural with PbTaSe₂. Although they have similar electronic structures, the nodal lines in these two materials come from different origins. The nodal lines in non-centrosymmetric PbTaSe₂ are protected by mirror reflection symmetry [21], while the nodal lines in SnTaS₂ are protected by time-reversal and inversion symmetries. The different symmetries cause that, when SOC is considered, the nodal lines are persistent in PbTaSe₂ but gapped in SnTaS₂ [21]. These properties in common with and differing from those of PbTaSe₂ make SnTaS₂ a great platform to further investigate the properties of superconducting nodal line semimetals.

IV. CONCLUSION

In summary, we report the magnetic, transport, and specific heat properties and the electronic structure of the centrosymmetric compound SnTaS₂, which is a layered type-II superconductor. Large anisotropy is found in the upper critical field and the GL coherence length. An obvious upward curvature is observed in the upper critical field curve for $H//ab$, maybe due to the multiband effect or the nonlocal effect, which needs further investigation to clarify. The electron-phonon coupling constant is determined to be 0.66, indicating a moderately coupled superconductor. The band structure of SnTaS₂ exhibits three nodal lines in the $k_z = 0$ plane near the Fermi level with drumheadlike surface states. With a crystal structure similar to that of PbTaSe₂ but symmetries different from those of noncentrosymmetric PbTaSe₂, SnTaS₂ is considered a promising system to research the novel properties of superconducting topological nodal line semimetals.

ACKNOWLEDGMENTS

This work was supported by the National Natural Science Foundation of China (Grants No. 11804176 and No. 11734003), the National Key Research and Development Program of China (Grant No. 2016YFA0300604), Shandong Provincial Natural Science Foundation, China (Grant No. ZR2018BA030), and China Postdoctoral Science Foundation (Grant No. 2018M632609).

- [1] X.-L. Qi and S.-C. Zhang, *Rev. Mod. Phys.* **83**, 1057 (2011).
- [2] L. Fu and C. L. Kane, *Phys. Rev. Lett.* **100**, 096407 (2008).
- [3] M. Z. Hasan and C. L. Kane, *Rev. Mod. Phys.* **82**, 3045 (2010).
- [4] H. Zhang, C.-X. Liu, X.-L. Qi, X. Dai, Z. Fang, and S.-C. Zhang, *Nat. Phys.* **5**, 438 (2009).
- [5] N. P. Armitage, E. J. Mele, and A. Vishwanath, *Rev. Mod. Phys.* **90**, 015001 (2018).
- [6] Z. Wang, Y. Sun, X.-Q. Chen, C. Franchini, G. Xu, H. Weng, X. Dai, and Z. Fang, *Phys. Rev. B* **85**, 195320 (2012).
- [7] H. Weng, C. Fang, Z. Fang, B. A. Bernevig, and X. Dai, *Phys. Rev. X* **5**, 011029 (2015).
- [8] A. A. Soluyanov, D. Gresch, Z. Wang, Q. Wu, M. Troyer, X. Dai, and B. A. Bernevig, *Nature (London)* **527**, 495 (2015).
- [9] L. M. Schoop, M. N. Ali, C. Straer, A. Topp, A. Varykhalov, D. Marchenko, V. Duppel, S. S. P. Parkin, B. V. Lotsch, and C. R. Ast, *Nat. Commun.* **7**, 11696 (2016).
- [10] X. Zhang, Z.-M. Yu, Z. Zhu, W. Wu, S.-S. Wang, X.-L. Sheng, and S. A. Yang, *Phys. Rev. B* **97**, 235150 (2018).
- [11] H. Weng, C. Fang, Z. Fang, and X. Dai, *Phys. Rev. B* **93**, 241202(R) (2016).
- [12] Y. S. Hor, A. J. Williams, J. G. Checkelsky, P. Roushan, J. Seo, Q. Xu, H. W. Zandbergen, A. Yazdani, N. P. Ong, and R. J. Cava, *Phys. Rev. Lett.* **104**, 057001 (2010).
- [13] Z. Liu, X. Yao, J. Shao, M. Zuo, L. Pi, S. Tan, C. Zhang, and Y. Zhang, *J. Am. Chem. Soc.* **137**, 10512 (2015).

- [14] Y. Qiu, K. N. Sanders, J. Dai, J. E. Medvedeva, W. Wu, P. Ghaemi, T. Vojta, and Y. S. Hor, [arXiv:1512.03519](#).
- [15] K. Kirshenbaum, P. S. Syers, A. P. Hope, N. P. Butch, J. R. Jeffries, S. T. Weir, J. J. Hamlin, M. B. Maple, Y. K. Vohra, and J. Paglione, *Phys. Rev. Lett.* **111**, 087001 (2013).
- [16] L. He, Y. Jia, S. Zhang, X. Hong, C. Jin, and S. Li, *npj Quantum Mater.* **1**, 16014 (2016).
- [17] D. Kang, Y. Zhou, W. Yi, C. Yang, J. Guo, Y. Shi, S. Zhang, Z. Wang, C. Zhang, S. Jiang *et al.*, *Nat. Commun.* **6**, 7804 (2015).
- [18] X.-C. Pan, X. Chen, H. Liu, Y. Feng, Z. Wei, Y. Zhou, Z. Chi, L. Pi, F. Yen, F. Song *et al.*, *Nat. Commun.* **6**, 7805 (2015).
- [19] Y. Qi, P. G. Naumov, M. N. Ali, C. R. Rajamathi, W. Schnelle, O. Barkalov, M. Hanfland, S.-C. Wu, C. Shekhar, Y. Sun *et al.*, *Nat. Commun.* **7**, 11038 (2016).
- [20] M. N. Ali, Q. D. Gibson, T. Klimczuk, and R. J. Cava, *Phys. Rev. B* **89**, 020505(R) (2014).
- [21] G. Bian, T.-R. Chang, R. Sankar, S.-Y. Xu, H. Zheng, T. Neupert, C.-K. Chiu, S.-M. Huang, G. Chang, I. Belopolski *et al.*, *Nat. Commun.* **7**, 10556 (2016).
- [22] F. J. Di Salvo, G. W. Hull, Jr., L. H. Schwartz, J. M. Voorhoeve, and J. V. Waszczak, *J. Chem. Phys.* **59**, 1922 (1973).
- [23] J. Dijkstra, E. A. Broekhuizen, C. F. van Bruggen, C. Haas, R. A. de Groot, and H. P. van der Meulen, *Phys. Rev. B* **40**, 12111 (1989).
- [24] G. Kresse and D. Joubert, *Phys. Rev. B* **59**, 1758 (1999).
- [25] J. P. Perdew, K. Burke, and M. Ernzerhof, *Phys. Rev. Lett.* **77**, 3865 (1996).
- [26] Q. Wu, S. Zhang, H.-F. Song, M. Troyer, and A. A. Soluyanov, *Comput. Phys. Commun.* **224**, 405 (2018).
- [27] E. H. Brandt, *Phys. Rev. B* **60**, 11939 (1999).
- [28] C.-L. Zhang, Z. Yuan, G. Bian, S.-Y. Xu, X. Zhang, M. Z. Hasan, and S. Jia, *Phys. Rev. B* **93**, 054520 (2016).
- [29] Y.-J. Long, L.-X. Zhao, P.-P. Wang, H.-X. Yang, J.-Q. Li, H. Zi, Z.-A. Ren, C. Ren, and G.-F. Chen, *Chin. Phys. Lett.* **33**, 037401 (2016).
- [30] J. Wang, X. Xu, N. Zhou, L. Li, X. Cao, J. Yang, Y. Li, C. Cao, J. Dai, J. Zhang *et al.*, *J. Supercond. Novel Magn.* **28**, 3173 (2015).
- [31] R. A. Klemm, A. Luther, and M. R. Beasley, *Phys. Rev. B* **12**, 877 (1975).
- [32] Y. N. Ovchinnikov and V. Z. Kresin, *Phys. Rev. B* **52**, 3075 (1995).
- [33] S. Maekawa, H. Ebisawa, and H. Fukuyama, *J. Phys. Soc. Jpn.* **52**, 1352 (1983).
- [34] A. Gurevich, *Phys. Rev. B* **67**, 184515 (2003).
- [35] G. Kotliar and C. M. Varma, *Phys. Rev. Lett.* **77**, 2296 (1996).
- [36] P. C. Hohenberg and N. R. Werthamer, *Phys. Rev.* **153**, 493 (1967).
- [37] D. E. Prober, R. E. Schwall, and M. R. Beasley, *Phys. Rev. B* **21**, 2717 (1980).
- [38] R. V. Coleman, G. K. Eisman, S. J. Hillenius, A. T. Mitchell, and J. L. Vicent, *Phys. Rev. B* **27**, 125 (1983).
- [39] J. R. Clem, *Phys. C (Amsterdam, Neth.)* **162**, 1137 (1989).
- [40] W. L. McMillan, *Phys. Rev.* **167**, 331 (1968).
- [41] X. Zhang, Z.-M. Yu, X.-L. Sheng, H. Y. Yang, and S. A. Yang, *Phys. Rev. B* **95**, 235116 (2017).
- [42] Y. Kim, B. J. Wieder, C. L. Kane, and A. M. Rappe, *Phys. Rev. Lett.* **115**, 036806 (2015).
- [43] R. Yu, H. Weng, Z. Fang, X. Dai, and X. Hu, *Phys. Rev. Lett.* **115**, 036807 (2015).
- [44] X. Zhang, L. Jin, X. Dai, and G. Liu, *J. Phys. Chem. Lett.* **8**, 4814 (2017).
- [45] A. Yamakage, Y. Yamakawa, Y. Tanaka, and Y. Okamoto, *J. Phys. Soc. Jpn.* **85**, 013708 (2016).